JOURNAL OF GEOPHYSICAL RESEARCH, VOL. 104, NO. C2, PAGES 3243–3263, FEBRUARY 15, 1999

Bound waves and Bragg scattering in a wind-wave tank

William J. Plant,[1] William C. Keller,[1] Vahid Hesany,[1] Tetsu Hara,[2]
Erik Bock,[3] and Mark A. Donelan,[4,5]

Abstract. We present optical and microwave measurements that show the presence of bound waves traveling at the speed of the dominant wave in a wind-wave tank. We suggest that when these bound waves are much shorter than the dominant waves, they are preferentially located on the leeward face of the dominant wave and hence have a mean tilt. We hypothesize that the turbulence associated with these bound waves suppresses freely propagating, wind-generated waves where bound waves are present so that we may divide the rough water surface into patches containing free and patches containing bound waves. This model is shown to account for the observed histograms of slope measured in the tank and, at least qualitatively, for the observed decrease in the probability of finding bound waves with increasing wind speed. Furthermore, if we add these bound, tilted waves to the free waves of the standard Bragg/composite-surface scattering model for microwave scattering from rough water surfaces, then the model can account for many otherwise unexplained features of the scattering. Principal among these features are the rapid decrease in polarization ratio and rapid increase in the first moment of the microwave Doppler spectrum with increasing wind speed when the antenna is directed upwind, features that occur to a much lesser extent when the antenna looks downwind.

1. Introduction

Many investigators have noted that when microwave backscatter is observed in wind-wave tanks with the antenna directed into the wind, much of the backscatter is related to surface features that propagate at the speed of the dominant wave in the tank. This is especially true for high and low incidence angles, but the phenomenon is also apparent in backscattering at intermediate incidence angles [*Duncan et al.*, 1974; *Kwoh and Lake*, 1985; *Ebuchi et al.*, 1993; *Rozenberg et al.*, 1995]. While the nature of this backscatter has not been identified, its cause is widely accepted to be surface roughness on the leeward face of the dominant wave. Photographs of mechanically generated, short gravity waves in wave tanks as they approach breaking clearly show capillary waves being generated on the forward face of the crest [*Duncan et al.*, 1994a, b]. Similarly, photographs of wind-generated waves in wave tanks show such structures on the leeward face of the dominant waves [*Okuda et al.*, 1976; *Ebuchi et al.*, 1987; *Keller et al.*, 1995]. *Longuet-Higgins* [1992] points out that these structures may be higher-order effects than those accounted for by his 1963 theory of parasitic waves [*Longuet-Higgins*, 1963] since they contain high levels of vorticity. The work of *Okuda et al.* [1976], who use hydrogen bubbles to produce visualization of the flow beneath the water surface, makes this vorticity especially evident. Longuet-Higgins suggests that vorticity may be fed back from the capillary waves into the parent short gravity wave to cause a gently spilling breaker; such breaking need not be accompanied by a miniature plunging breaker or by air entrainment [*Longuet-Higgins*, 1992; *Longuet-Higgins and Cleaver*, 1994; *Longuet-Higgins*, 1994].

Thus while the region just ahead of the crest of a gently breaking short gravity wave may be an area of high turbulence, it need not be accompanied by an excessively rough surface on capillary wave scales. In this paper, we postulate that the high turbulence levels in these rough patches suppress wind-generated capillary waves, so that the total capillary wave field consists of patches of freely propagating, wind-generated waves that are spread more or less evenly over surface areas with low to moderate slopes and patches of bound waves that lie preferentially on the leeward face of the dominant wave, so that they have substantial mean slopes. We present evidence obtained in a wind-wave tank to support the view that these rough patches of bound, tilted waves scatter incident microwave signals

[1]Applied Physics Laboratory, University of Washington, Seattle.
[2]Graduate School of Oceanography, University of Rhode Island, Narragansett.
[3]Woods Hole Oceanographic Institution, Woods Hole, Massachusetts.
[4]Rosenstiel School of Marine and Atmospheric Science, University of Miami, Miami, Florida.
[5]Also at Environment Canada, Toronto, Ontario.

Paper number 1998JC900061.
0148-0227/99/1998JC900061$09.00

according to Bragg/ composite-surface scattering theory. From wave slope variance spectra as a function of uptank wavenumber and frequency obtained from a laser slope gauge, we obtain information on the relative spectral densities of free and bound waves as a function of along-tank wavenumber [*Bock and Hara*, 1995; *Hara et al.*, 1997]. From measurements of uptank and cross-tank slopes at a point we obtain expressions for the mean and variance of the slopes of free and bound waves. We also obtain estimates of the probability of observing free and bound waves as a function of friction velocity from these data. We show that the principal features of microwave measurements obtained in the tank at incidence angles of 45° and 55° can be explained by using the parameters obtained from the spectral and slope measurements in a Bragg/composite-surface scattering model that includes both free and bound waves.

2. Experiments

We carried out two sets of experiments in the recirculating wind-wave tank of the Canada Centre for Inland Waters (CCIW), one in 1993 and one in 1996. Figure 1 shows the experimental setup. The scanning laser slope gauge shown in the figure was not present in 1996. In 1993 the microwave antennas were fixed at a 45° incidence angle looking upwind, while in 1996 they were directed both upwind and downwind and were set at incidence angles of 35°, 45°, and 55°. Near the end of the experiment we discovered that data collected at 35° were contaminated by scattering from the edge of the Teflon window through which the antenna observed the surface. Thus data at 35° are not given in this paper. When looking upwind at 45° and 55°, the microwave footprint on the water was at a fetch of 10 m, and looking downwind, it was at 12.5 m. The inside roof and sides of the wind tunnel were lined with microwave absorbing material to a distance of 2.4 m upwind and 1.8 m downwind. The width of the tank was 76 cm. In 1993 the measurements reported here were made under steady wind conditions. In 1996 the wind was increased slowly from zero to a maximum wind speed, then reduced to zero at the same rate. For the 1996 measurements reported here, the friction velocity was increasing at a rate of 1 m/s in 60 min.

The scanning laser slope gauge has been described in detail by *Bock and Hara* [1995] and is the same one that was used by *Hara et al.* [1997]. Briefly, the system illuminates the water surface from below with a scanning laser beam, and the position of the refracted beam is measured by a detector above the air channel. The laser beam scans one 0.154 m diameter circle in 2.4 ms, surface slopes are measured at 129 locations around the circle in two scans, and the procedure is repeated every 14.4 ms. These slopes are cross-correlated in pairs to produce a two-dimensional representation of the autocorrelation function of the surface slope, which is transformed to yield the wave slope variance spectrum as a function of both angular frequency ω and wavenumber $\mathbf{k}$, i.e., $S(\mathbf{k},\omega)$. The Nyquist frequency of the system is 34.7 Hz, and the system responds to wavenumbers in the range from 20.4 to 800 rad/m.

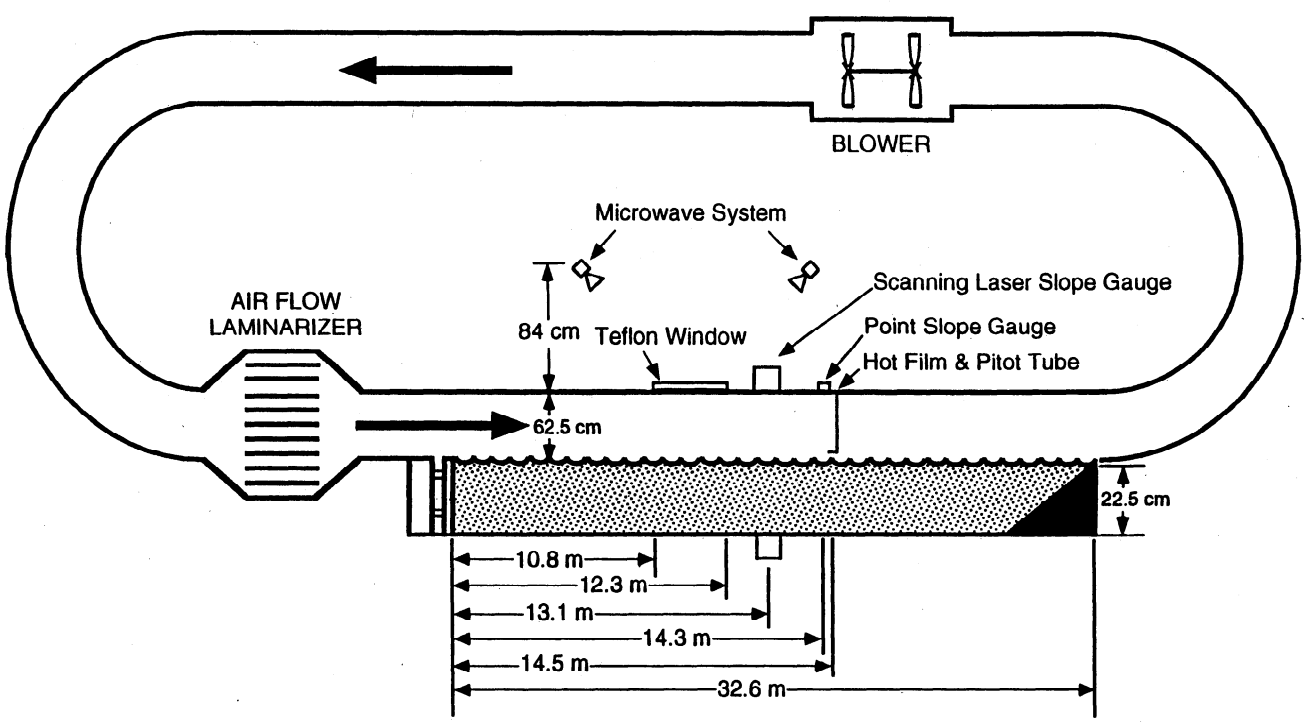

Figure 1. Diagram of the recirculating wind-wave tank of the Canada Centre for Inland Waters showing the location of the instruments used in this study.

The point slope gauge was similar to the scanning system except that it did not scan and used a higher-power laser. Thus the point slope gauge had a much higher signal-to-noise ratio than the scanning one and could detect all frequencies of motion of the surface up to a maximum determined by the spot size of the beam on the water surface and the sampling frequency, which was both 20 and 1000 Hz. The spot size was about 1 mm, so wavenumbers up to about 3000 rad/m could be measured. However, for the data shown in this paper, the 20 Hz sampling rate was used, so the effective maximum wavenumber was probably somewhat lower than this. The maximum power output of the laser was 3 W, but only 2 W were used in operation. The laser beam was directed horizontally below the tank and reflected upward through the tank bottom by a mirror. A Fresnel lens and detector above the tank recorded the position of the laser beam after it was refracted by the water surface. The maximum slope that could be measured by the system was 42°. From the slope spectra obtained from this point slope gauge, the frequency of the dominant wave in the tank could be determined.

The microwave system was identical to that described in detail by *Plant et al.* [1994] except that the frequency had been shifted up to Ku band; it is exactly the same system used by *Plant* [1997]. Briefly, the system was a coherent, dual-polarized, continuous wave system and data were collected on horizontal transmit/horizontal receive (HH) and vertical transmit/vertical receive (VV) polarizations simultaneously. Exact frequencies were 14.00 GHz for VV and 14.06 for HH. One-way half-power antenna beam widths were 6.6° in the E plane and 5.0° in the H plane, and the beam viewed the water surface through a 6 mm thick Teflon window. The height of the antennas was maintained at 146 cm above mean water level for all incidence angles and look directions. Calibration procedures differed slightly from those described by *Plant et al.* [1994] owing to the laboratory setting. Water was drained from the tank, and a corner reflector was placed on absorbing material on the bottom of the tank at various positions in the beam. Return from the corner reflector was measured as a function of position in the beam and used to calculate calibration constants as described by *Plant et al.* [1994]. In addition, illuminated areas could be calculated since return power as a function of position was measured. We found these areas to be accurately given by

$$A = \pi a^2 / \cos\theta \tag{1}$$

where θ is incidence angle and a is 13 cm for VV and 15 cm for HH polarization. Microwave return was collected at a sample rate of 257 Hz to fill an array 1024 samples long in 4 s. This array was then Fourier transformed to produce Doppler spectra that were stored on optical disks. A reference signal from the microwave system and the mean value of the sum of the squares of the inphase and quadrature channels were stored for later use in computing normalized radar cross sections σ_o.

Winds in the tank were measured using a pitot tube and a hot film anemometer, from which friction velocities could be calculated. The height of the pitot tube varied from 3 to 10 cm above the waver surface during the experiments, and the hot film was 3.2 cm directly above the pitot tube. Friction velocities quoted here have been corrected to be those at the surface. Air and water temperatures were recorded during each run, and the water surface was skimmed free of surfactants each morning before the runs began.

3. Wave Spectra

Figure 2 shows cuts through the spectra produced by the scanning laser slope gauge in a plane containing the frequency axis and the uptank wavenumber axis at four different friction velocities u_*. These data were taken on April 14, 1993, at a series of steady wind speeds. The left half of each spectrum is the alias of the right half. Solid lines are drawn through the origin and the dominant wave peak and clearly show that a ridge in the contour plots exists along these lines at some wind speeds. We identify these waves as bound waves. The dotted lines show the free wave dispersion relation if wind effects are ignored, while the dashed line shows the dispersion relation according to *Plant and Wright* [1980], which includes the effect of the wind drift layer on the frequency of the waves. Figure 2 indicates that a ridge of the contour plot is also located along this latter dispersion relation. We identify these waves as the freely propagating waves.

For each wavenumber we divided the frequency range into parts corresponding to free and bound waves. To do this, we chose a range from the midpoint between the free and bound wave dispersion relations to a point a fixed perpendicular distance above the bound wave dispersion relation to call the bound wave system. This region is illustrated in Figure 3 by the plus signs overlaid on the spectrum. Similarly, the region from the midpoint between the dispersion relations down to a fixed perpendicular distance below the free wave dispersion relation is denoted the free wave system. This is illustrated by the dots in Figure 3. We then integrated over the frequency ranges bounded by these regions for each uptank wavenumber and multiplied by the value of this wavenumber squared to get a value for the degree of saturation $B(k, 0)$ associated with each system. Figure 4 shows the result at four different friction velocities. The circles show bound wave values, while the asterisks give the free wave ones. The solid and dashed lines are used in the microwave scattering calculations described in section 5. Clearly seen in Figure 4 is the dip in the degree of saturation commonly observed in wave tank spectra [*Wright and Keller*, 1971; *Jähne and Riemer*, 1990; *Hara et al.*, 1997]. This dip is

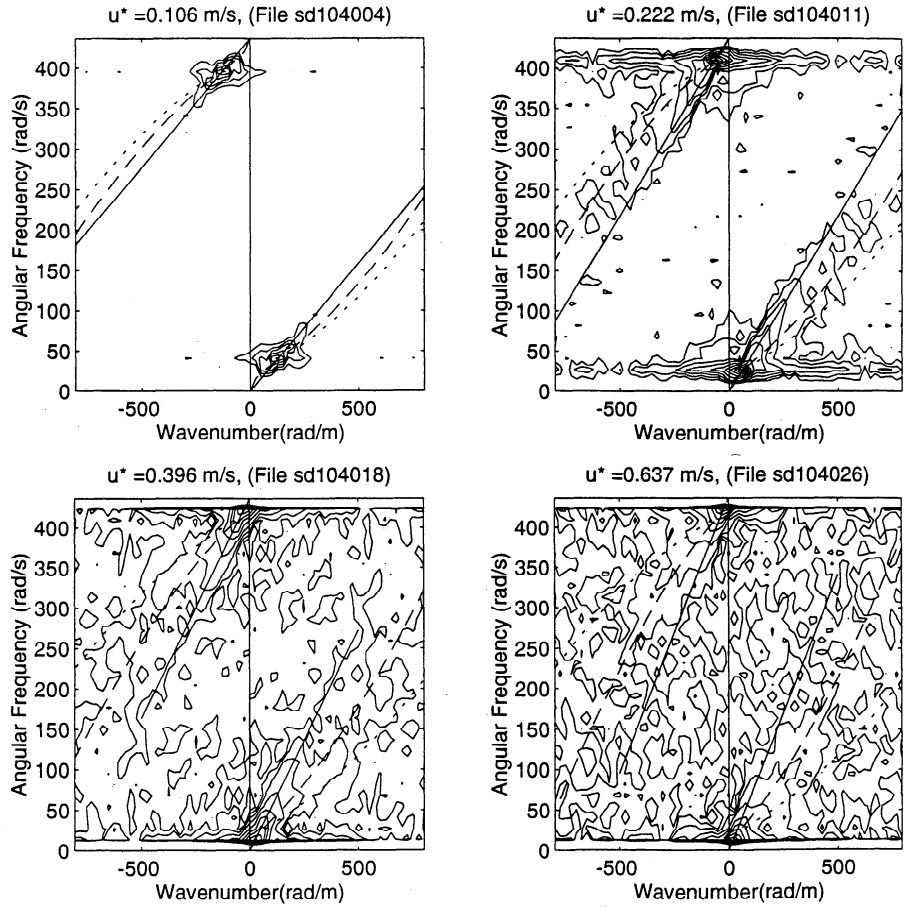

Figure 2. Wave slope variance spectra as a function of uptank wavenumber and angular frequency at various friction velocities $u*$ as measured by the scanning laser slope gauge. Solid lines are drawn through zero and the dominant wave peak. Dotted lines show the short wave dispersion relationship without wind, while dashed lines give the dispersion relationship including wind according to *Plant and Wright* [1980].

evident at low wind speeds but fills in at higher ones. Interestingly, however, at higher wind speeds the bound wave contribution to the total spectrum falls dramatically at wavenumbers below that which corresponds to the low point of the dip at low wind speeds, about 400 rad/m.

4. Wave Slopes

We now carry farther our division of the short wave system into bound and free components by examining histograms of the uptank and cross-tank slopes measured at a point. From our earlier discussion we expect the bound wave system to have a mean negative slope since it will be located on the leeward face of the dominant wave. Figure 5 shows histograms of the uptank and cross-tank slopes normalized to a value of 1 at the peak, along with our fits to them, which we discuss below. These data were collected on April 1, 1996, with the friction velocity slowly ramping up from 0 to 0.5 m/s in 30 min. Noticeable in Figure 5 is the excess number of fairly large negative slopes in the uptank histograms, which are absent in the cross-tank ones. We attribute these excess negative slopes to the rough regions where bound waves are found and separate them from the regions containing free waves by the following procedure. At slopes above its peak, the normalized histogram of slopes, given by the open circles in Figure 5, is fit to a Gaussian form

$$H_n = e^{-(s-<s>)^2/[2\mathrm{Var}(s)]} \tag{2}$$

where s is uptank or cross-tank slope, $< s >$ is its mean value, and $\mathrm{Var}(s)$ is its variance. The curve representing this fit is then extended to slopes below the peak to produce the dashed line in Figure 5. This line is then subtracted from the original data, the open circles, to produce residuals, the dots in Figure 5, which we interpret as the histogram of bound wave slopes. These residuals are then fit to the form (2) with an appropriate multiplying factor in front of the right side. This produces the thin solid line in Figure 5. Finally, the fits to the free waves, the dashed line, and the fit to the bound waves, the thin solid line, are added together to produce the thick solid line shown in Figure 5.

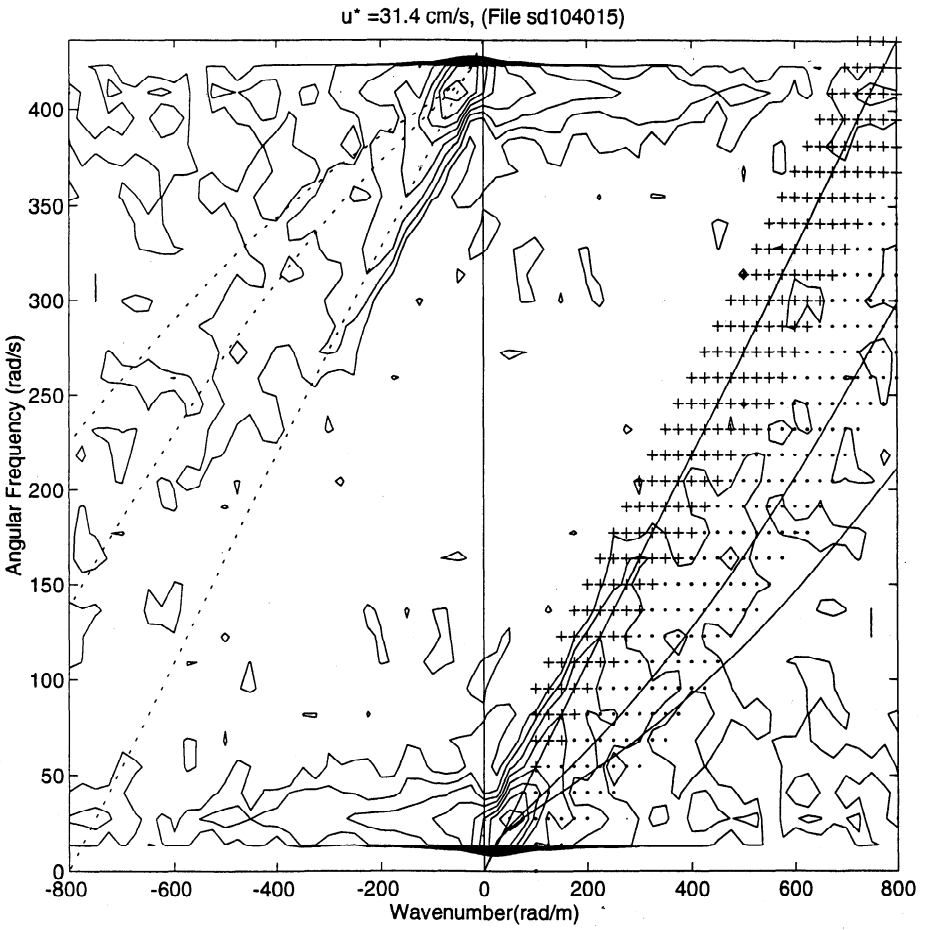

Figure 3. Wave slope variance spectra from the laser slope gauge at a friction velocity of 0.31 m/s showing the division between bound and free waves. The region marked by pluses was considered to be bound waves, while that covered by points was considered to be free waves.

From these fits we can extract values of the mean and variance of the uptank and cross-tank total slopes and of the uptank slopes in regions of free and bound waves. To be more specific about what we mean by these various slopes, let us consider our proposed rough-surface model in a bit more detail. We suppose that when rough patches containing bound waves are present on the surface, their turbulence suppresses short waves that are generated directly by the wind and are freely propagating. Thus we can divide the surface into patches where free waves exist and patches where bound waves exist. Then the total probability of finding a given slope angle (s_u, s_c), where subscripts u and c indicate uptank and cross-tank, respectively, on the surface is given by

$$P(s_u, s_c) = P_f P(s_u, s_c|f) + P_b P(s_u, s_c|b) \tag{3}$$

where P_f is the probability of finding a free wave in a given small patch, $P(s_u, s_c|f)$ is the distribution of slopes given that a free wave is present, and P_b and $P(s_u, s_c|b)$ are similar quantities for bound waves. Since uptank and cross-tank slopes are independent random variables, we may write (3) as

$$\begin{aligned} P(s_u, s_c) &= P_f P(s_u|f) P(s_c|f) \\ &+ P_b P(s_u|b) P(s_c|b) \end{aligned} \tag{4}$$

Since the integral of $P(s_u, s_c)$, $P(s_i|f)$, and $P(s_i|b)$, $i = u$ or c, over all slopes must be 1, this equation immediately and obviously implies that

$$P_f + P_b = 1. \tag{5}$$

It also implies a relationship between means and variances of total, bound, and free wave slopes from which P_f and P_b can be determined if means and variances are measured. Thus

$$< s_i >= P_f < s_i >_f + P_b < s_i >_b \tag{6}$$

where $< s_i >_f$ is the mean slope of the surface where free waves exist and $< s_i >_b$ is the mean slope where bound waves exist. From (6) it immediately follows that

$$P_f = \frac{< s_i > - < s_i >_b}{< s_i >_f - < s_i >_b} \tag{7}$$

and P_b can be calculated from (5). In a similar manner, we also have

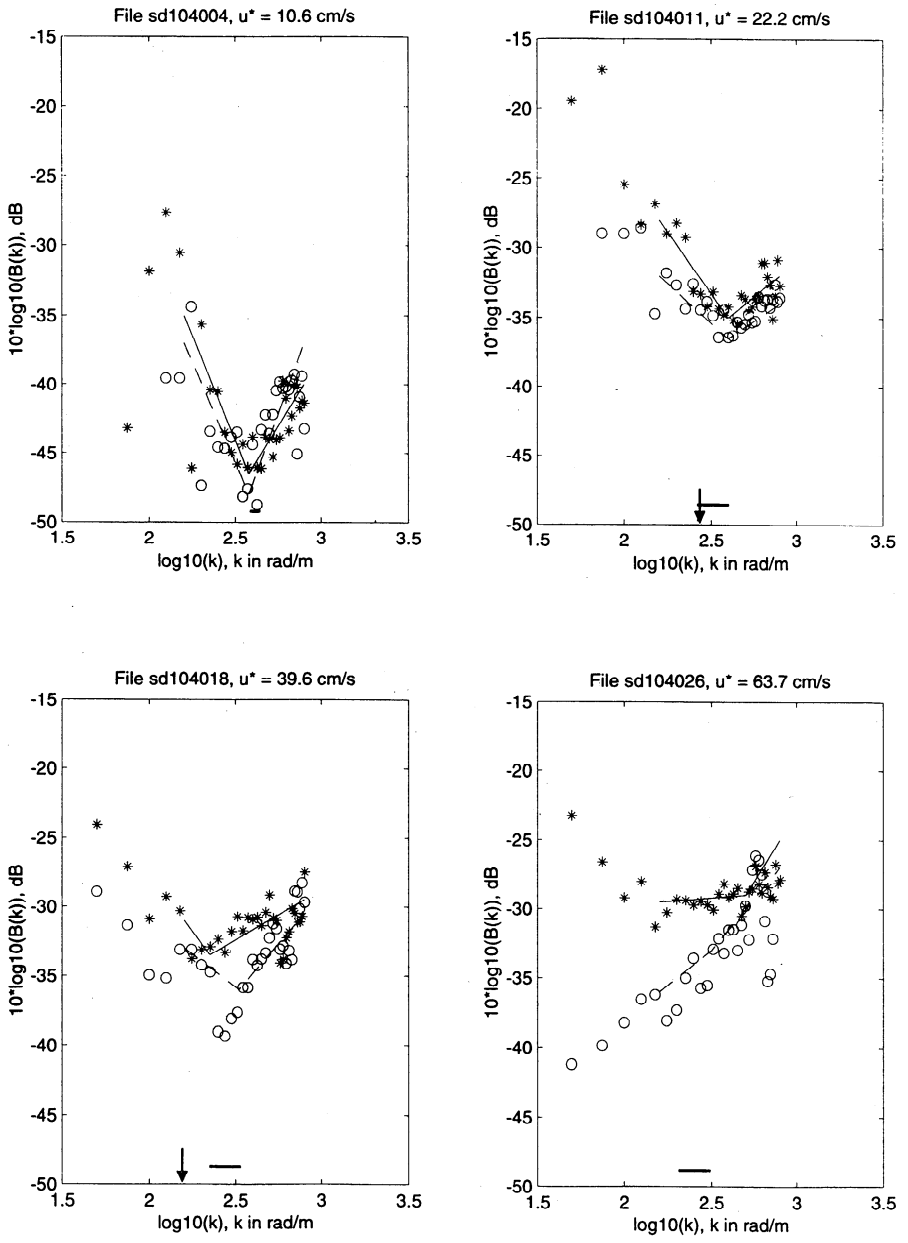

Figure 4. Degree of saturation of short waves propagating along the tank as a function of wavenumber in that direction for various friction velocities u_*. Circles indicate bound wave measurements, and the dashed line is the fit to them used as part of the microwave scattering calculations. Asterisks are free wave measurements, and the solid line is the fit to them used in the scattering calculations. Horizontal lines at the bottom show the region from which 90% of the scattering from bound waves comes when looking upwind at a 45° incidence angle. Arrows show 4 times the dominant wavenumber, the point above which the bound wave $B(k,0)$ used in the microwave scattering calculations is within 3 dB of the dashed lines; below 5 times the dominant wavenumber, we let the bound wave $B(k,0)$ fall linearly to zero at 3 times the dominant wavenumber. The arrow in the top left plot is offscale to the right, while that in the bottom right plot is offscale to the left.

$$P_f = \left[\mathrm{Var}(s_i) - \mathrm{Var}(s_i)_b - (< s_i >_b - < s_i >)^2\right] / \left[\mathrm{Var}(s_i)_f - \mathrm{Var}(s_i)_b + (< s_i >_f - < s_i >)^2 + (< s_i >_b - < s_i >)^2\right] \quad (8)$$

where $\mathrm{Var}(s_i)_f$ is the variance of slopes associated with free waves and $\mathrm{Var}(s_i)_b$ is that associated with bound waves.

Figure 6 gives as symbols the values of the various slopes obtained from our fits to slope histograms from our 1996 data and the values of P_f and P_b obtained from them. The lines in Figures 6a–6f are the functional forms used in our microwave scattering calculations to be discussed below. Several observations can be made about these data. First, while the mean slope

of patches containing bound waves becomes rapidly more negative with increasing wind speed as might be expected, patches containing free waves also have mean slopes that rapidly become positive at low winds before stabilizing or decreasing slightly (see Figure 6e). This behavior can be understood by noting that it is required by (6) if P_f and P_b are both nonzero. Alternatively, we can note that if the turbulence associated with bound waves suppresses free waves in areas of large negative slopes, then the mean slope of patches containing free waves must become somewhat positive. Second, it is interesting to note that while $\mathrm{Var}(s_u)_f$ increases monotonically with increasing wind speed, $\mathrm{Var}(s_u)_b$ decreases above about $u_* = 0.20$ m/s (see Figures 6c and 6d). This indicates that the patches where bound waves are located become less rough as the wind speed increases and the dominant wave increases in length. Finally, the crosses and pluses in Figure 6f are P_f and P_b, respectively, derived from (7), while the circled crosses and circled pluses are values derived from (8).

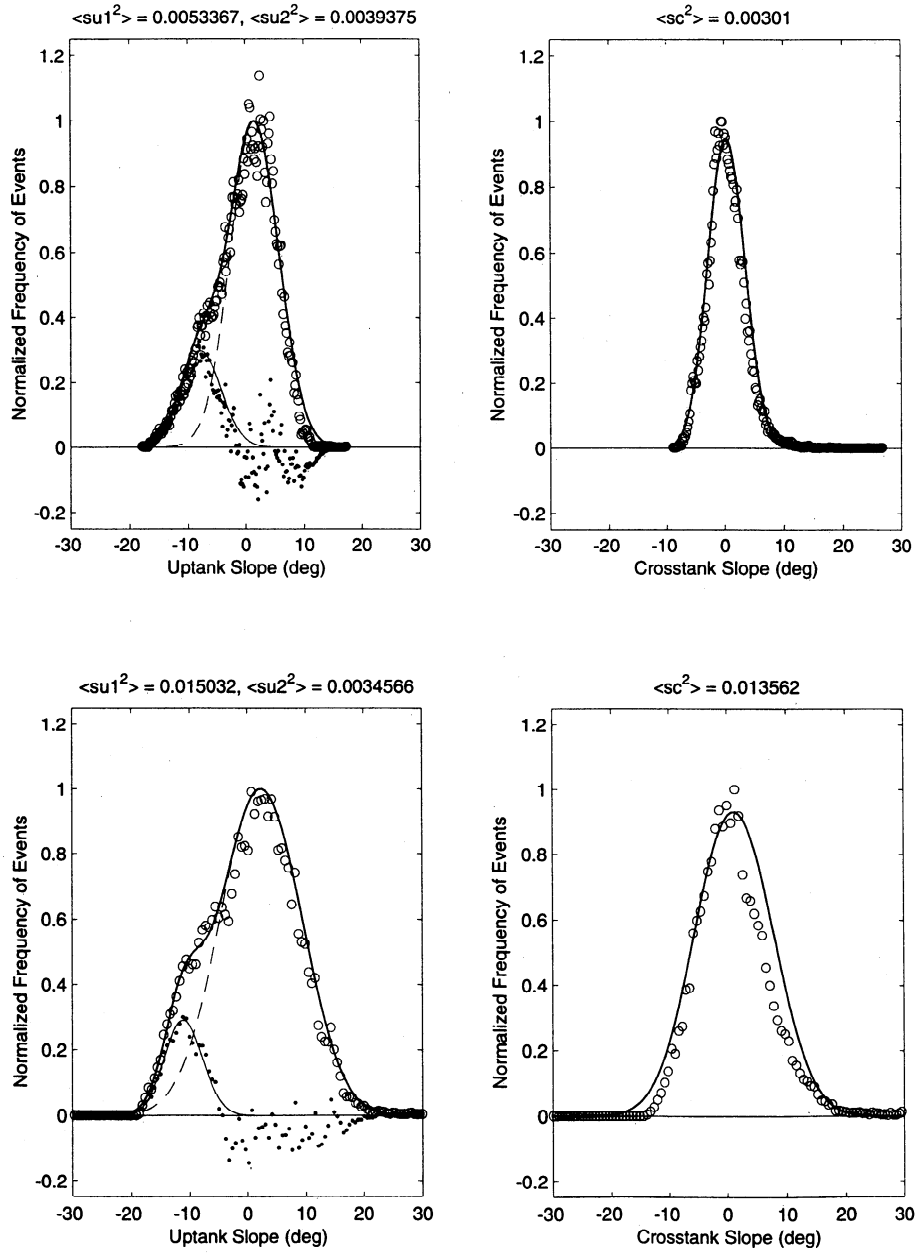

Figure 5. Histograms of uptank and cross-tank slopes normalized to 1 at the peak (open circles). Dashed line is a Gaussian fit to slopes higher than the peak of the histogram extended below the peak. The thin solid line is a Gaussian fit to the dots, which are obtained by subtracting the dashed line from the open circles. The thick solid line is the sum of the dashed and thin solid lines, which is our best fit to the data. We interpret the dashed line to be the best fit to the histogram of free waves, the thin solid line to be the same for bound waves, and the thick solid line to be this fit for the total slopes. Note that the bound waves were not found in the cross-tank slopes.

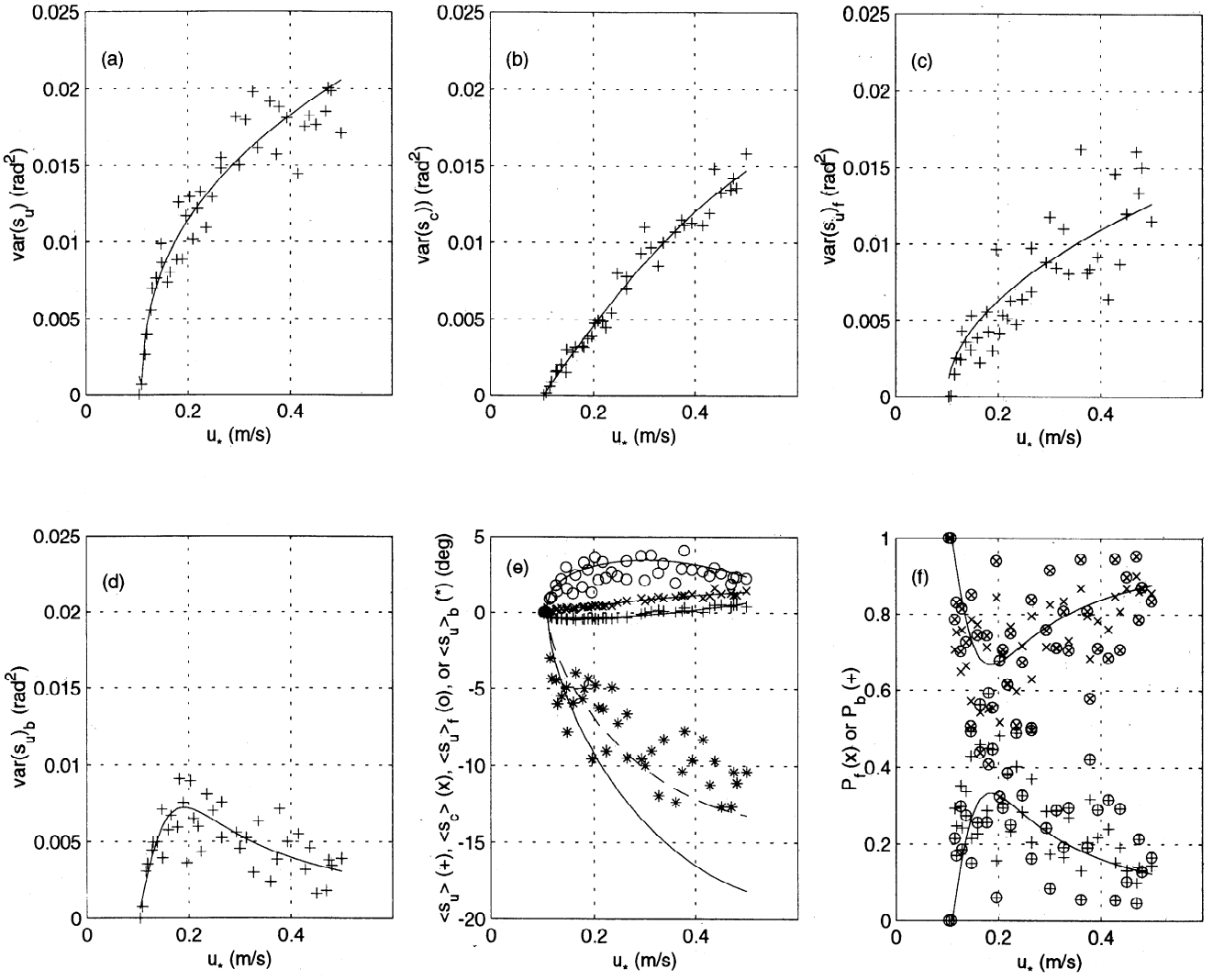

Figure 6. Parameters derived from the slope histograms of Figure 5 as a function of friction velocity. (a) Variance of total uptank slope. (b) Variance of total cross-tank slope. (c) Variance of the free wave part of the uptank slope. (d) Variance of the bound wave part of the uptank slope. (e) Mean slopes, with open circles denoting free wave uptank slope; pluses, total uptank slope; crosses, total cross-tank slope; and asterisks, bound wave uptank slope. (f) Probabilities of finding free (P_f) and bound (P_b) waves, with crosses denoting P_f from mean slopes; circled crosses, P_f from slope variances; pluses, P_b from mean slopes; and circled crosses, P_b from slope variances. Solid lines are functions used in the microwave scattering calculations. In Figure 6e the dashed line is $< s_u >_b$ used for downwind-looking antennas and the lowest solid line is $< s_u >_b$ used for upwind-looking antennas.

The latter set are more scattered as would be expected from a second-moment calculation, but the two sets of symbols agree with each other rather well and indicate that the probability of finding patches of bound waves maximizes at about $u_* = 0.18$ m/s and decreases at higher winds. This is perhaps understandable since as the wind speed increases, the turbulence associated with bound waves will become less able to suppress the wind waves. This will limit the area associated with bound wave patches. If these patches are associated with dominant wave crests and the dominant wavelength increases but the area of the patches does not, then the probability of detecting a bound wave should be expected to decrease as observed. In this case, the average length of a bound wave patch along the tank should be equal to the probability of finding such a patch multiplied by the dominant wavelength. Figure 7 shows the length of the dominant wave and the average length of a bound wave patch. The dominant wavelength was computed from measured dominant wave frequencies following *Plant and Wright* [1980] as described in more detail below. The figure shows that, indeed, the average length of a bound wave patch does maximize at about $u_* = 0.25$ cm/s. It is probably dangerous to extrapolate this behavior to the open ocean for reasons discussed in section 7, however.

5. Microwave Measurements

The reason that bound wave effects have been suspected by many investigators in wave tank backscattering measurements is illustrated in Figure 8, which shows Doppler spectra obtained at a 45° incidence angle in the CCIW tank on April 2, 1996. In these wave tank measurements some scattering from the roof and sides of the tank was observed at very low frequencies, even though these were covered with absorbing material. Therefore spectral densities have been set to zero for frequencies between ±15 Hz. Figures 8a and 8b show spectra looking upwind, while Figures 8c and 8d show those obtained looking downwind. The friction velocity was 0.47 m/s when these spectra were obtained. The expected positions of spectral peaks for scatterers moving at the speed of Bragg scatterers and the speed of the dominant wave are indicated by the arrows labeled "B" and "D," respectively. These frequencies were computed from the standard equation for the Doppler shift

$$f_d = \frac{k_B V}{2\pi} \tag{9}$$

where scatterers are assumed to move horizontally at a speed V and k_B is the Bragg resonance wavelength given by

$$k_B = \frac{4\pi \sin\theta}{\lambda} \tag{10}$$

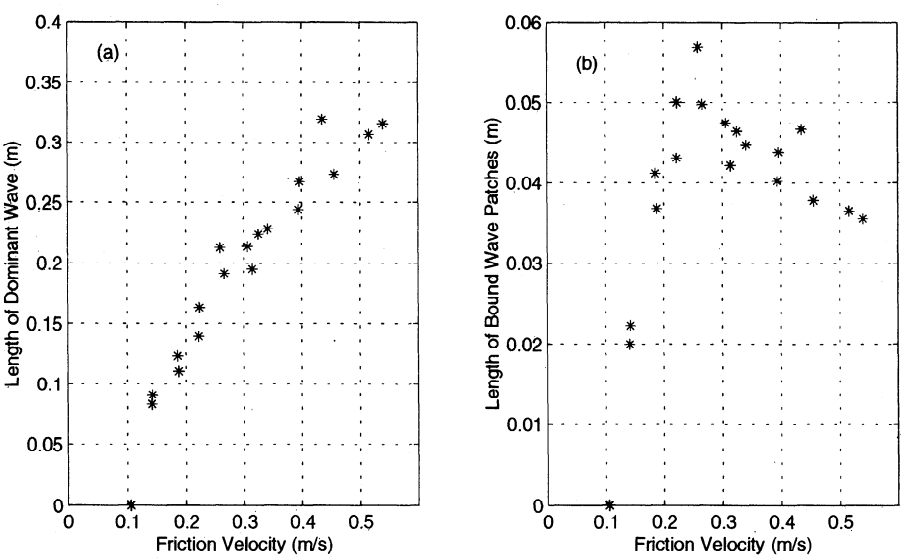

Figure 7. (a) Length of the dominant wave in the tank versus friction velocity. These were calculated from measured peak frequencies using the model of *Plant and Wright* [1980]. (b) Average length of a bound wave patch versus friction velocity.

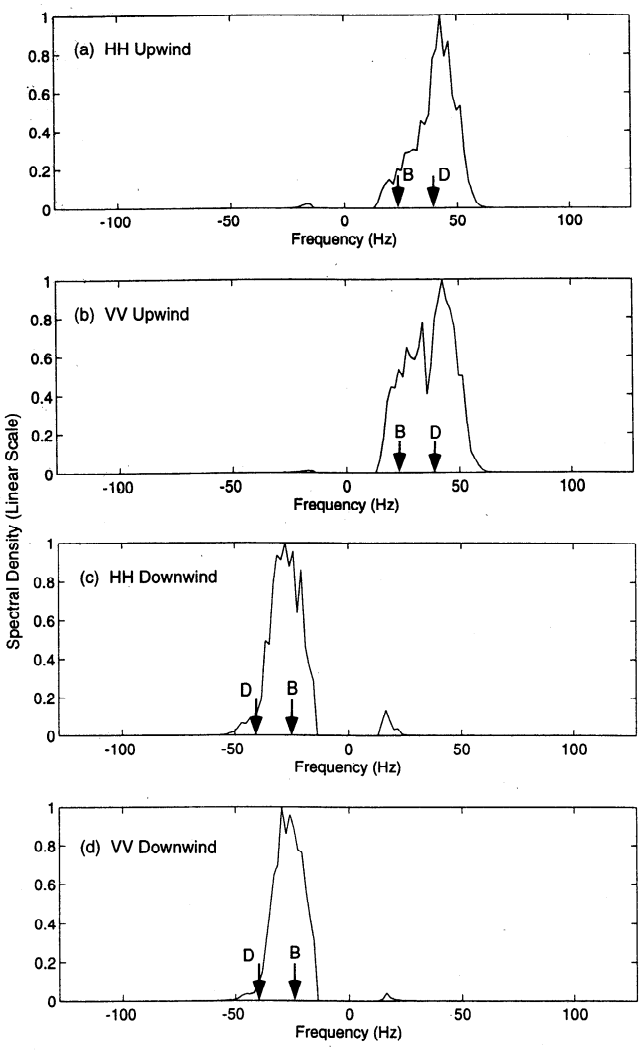

Figure 8. Doppler spectra measured in the wind-wave tank. (a) HH polarization with the antenna looking upwind. (b) VV polarization with the antenna looking upwind. (c) HH polarization with the antenna looking downwind. (d) VV polarization with the antenna looking downwind. Arrows labeled "B" show expected position of the free Bragg wave peak, while those labeled "D" give the expected position of the peak if the scatterer moves at the dominant wave phase speed.

where λ is microwave length. For V we have used the phase speed of the free Bragg or the dominant wave. In both cases we have applied the model of *Plant and Wright* [1980] using a surface drift $U_s = 0.6u*$ and a roughness length in the water of 0.004 cm to obtain this speed. For the Bragg wave, (10) gives the wavenumber of the wave for input to the model, while for the dominant wave the peak frequency as measured by the wave gauge was used as input. From Figure 8 it is rather clear that the peak of the spectrum is near the position expected for a scatterer moving at the speed of the dominant wave when the antenna is directed upwind, while it is near the position expected for the Bragg wave when the antenna is looking downwind.

Figure 9 shows data collected looking upwind with an incidence angle of 45° on April 14, 1993, as a function of wind speed. Figures 9a and 9b show measured normalized cross sections σ_o for both VV and HH polarizations, respectively, while Figure 9c gives their ratio, $\sigma_o(\mathrm{VV})/\sigma_o(\mathrm{HH})$ in decibels. Figure 9d gives the position of the peak of the Doppler spectrum (circled asterisks and pluses) and its first moment f_1 (asterisks and pluses), defined by

$$f_1 = \frac{\int fS(f)df}{\int S(f)df} \tag{11}$$

where $S(f)$ is the Doppler spectral density. The solid line in Figure 9 gives the expected position of the spectral peak, computed as outlined above, if the scatterer moves at the dominant wave speed, and the dashed line gives the peak position if the scatterer is a free Bragg wave. Figure 9 shows that, while the spectral peak is close to that expected from a scatterer moving with the dominant wave, f_1 is well below that value. This indicates that other parts of the Doppler spectrum away from the peak contribute significantly to the first-moment calculation. Since f_1 is below the value expected from the dominant wave alone, this suggests that a slower-moving scatterer such as the free Bragg wave is also producing significant backscatter and since f_1 for VV polarization falls below that for HH, the free Bragg wave probably plays a larger role for VV polarization than for HH.

The polarization ratio, however, really gives the clue that the scattering may be a combination of that due to a bound, tilted scatterer moving with the dominant wave and the free Bragg wave. At a 45° incidence angle the expected polarization ratio for pure Bragg scattering is 8 dB. As shown below, adding tilting and advection due to the longer waves according to the composite surface theory changes this ratio slightly, but it cannot explain the drop of more than 4 dB shown in Figure 9c as the wind speed increases. This drop could be explained, however, if a bound, tilted wave contributed to the scattering process according to Bragg scattering theory. This is because its location on the leeward face of the dominant wave would cause the local incidence angle to decrease, which, according to Bragg scattering theory, decreases the polarization ratio. For this reason, we attempted to determine whether a composite surface model including both free and bound, tilted Bragg waves could account for the observed backscatter.

As a first step in this attempt, we carried out measurements with the antenna looking both upwind and downwind in 1996. The larger symbols in Figures 10 through 13 show results from these measurements similar to those from 1993 shown in Figure 9. The smaller symbols are the predictions of the Bragg/composite-surface model discussed in section 6. The main difference between the data sets in 1993 and 1996, other than the downwind measurements in 1996, was the fact that the wind speed was slowly increasing in 1996 while it was constant in 1993. Two observations are

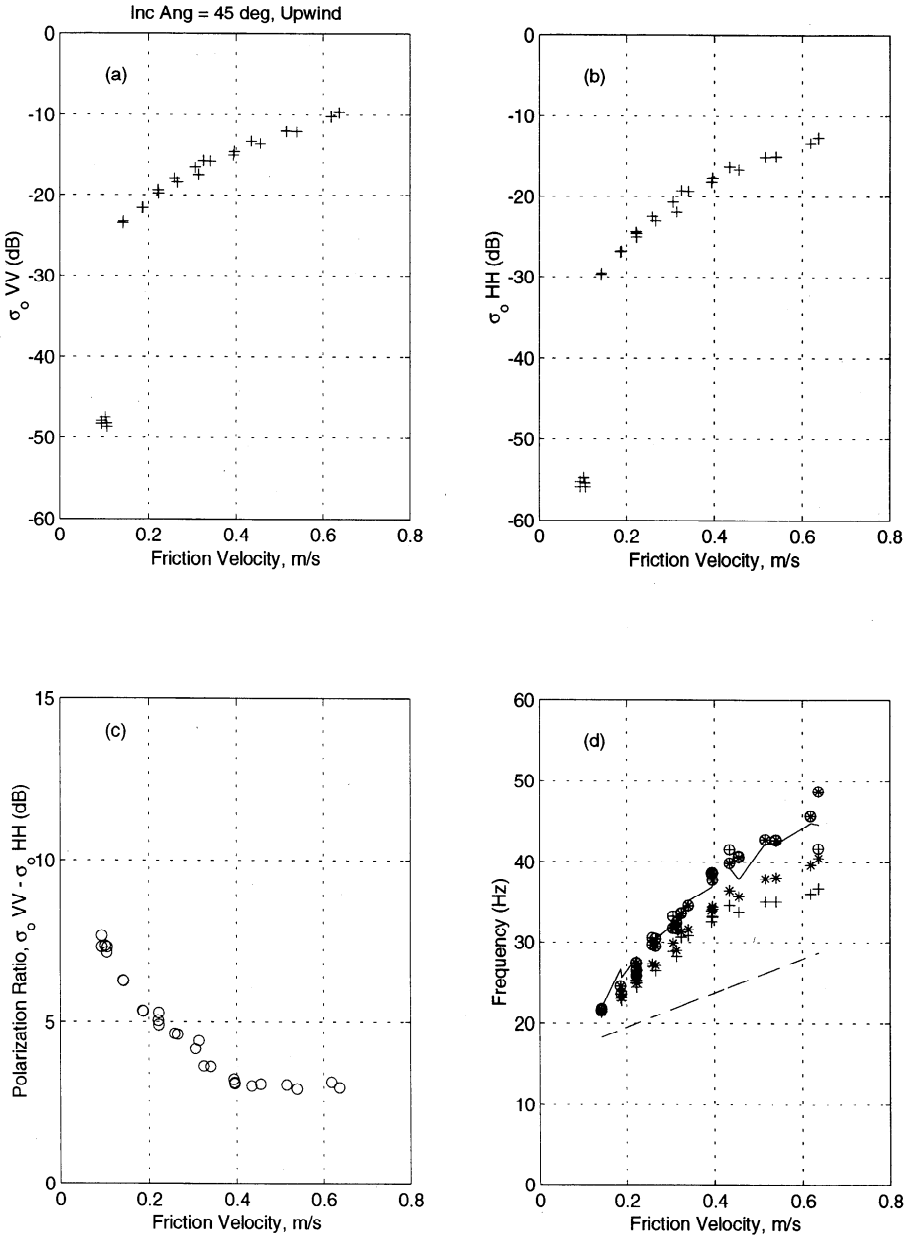

Figure 9. Microwave backscatter data taken at a 45° incidence angle looking upwind on April 14, 1993, versus friction velocity. (a) Normalized radar cross section σ_o for VV polarization. (b) The σ_o for HH polarization. (c) Polarization ratio, σ_o(VV)/ σ_o(HH). (d) Peak frequency f_p and first moment f_1, of Doppler spectra. In Figure 9d, asterisks denote f_1 and HH; pluses, f_1 and VV; circled asterisks, f_p and HH; and circled pluses, f_p and VV. Solid line is the shift expected from a scatterer traveling at the dominant wave phase speed, and the dashed line is the shift due to a free Bragg scatterer.

striking when comparing the upwind and downwind results shown in Figures 10–13. First, while the polarization ratio does decrease somewhat with increasing wind speed when the antenna is pointed downwind, this decrease is far smaller than in the case of upwind-looking antennas. This is again suggestive of the combined effects of free and bound, tilted Bragg waves since, when looking downwind, the tilted waves would occur at a larger local incidence angle and therefore contribute less to the backscatter than in the upwind case. This, in turn, would make the polarization ratio behave more like that in the case of composite-surface scattering from only free Bragg waves. Second, the first moment of the Doppler spectrum increases with wind speed much less in the case of downwind looks than when the antenna looks upwind. Again, this is indicative of the decreased importance of the bound waves when looking in this direction. In the next section we define this model more quantitatively by incorporating the results of the spectral and slope measurements.

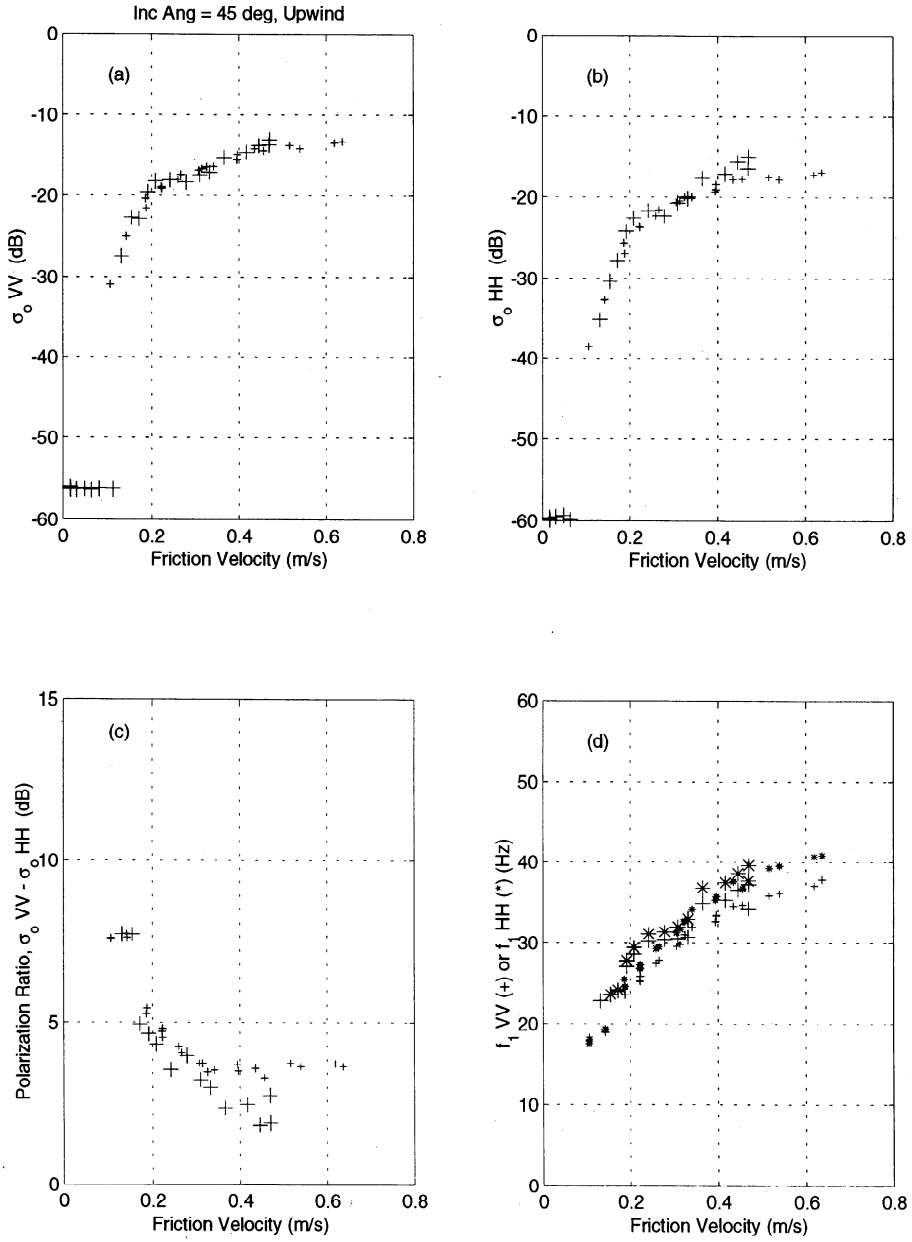

Figure 10. Large symbols are same as Figure 9, except for data taken in 1996. The smaller symbols are the predictions of Bragg/composite-surface theory for the total backscatter including both free and bound waves. Only first moments are shown in Figure 10d, where asterisks denote HH and pluses represent VV.

6. A Bragg/Composite-Surface Model

Bragg/composite-surface scattering theory was developed to remove the requirement of slightly rough perturbation theory (simple Bragg scattering theory) that the product of the vertical component of the microwave number times the surface displacement be small. It postulates that the rough water surface is slightly rough over small scales and that the large-scale waves may be treated by a tangent plane approximation in which they tilt and advect the small-scale Bragg scattering waves but, at moderate incidence angles, do not themselves contribute to the scattering. As ordinarily applied, composite-surface theory treats the small-scale waves as freely propagating, wind-generated waves. Here we want to add effects due to a second type of small-scale wave that is generated by a parent short gravity wave, propagates with that short gravity wave, and exists primarily on the leeward face of the parent wave, so that it exhibits a mean tilt angle that is not zero. Some problems exist when applying such a model to a wind-wave tank situation because at low wind speeds, the dominant wave in the tank, which we suppose to be the parent wave, is not much longer than the bound wave, which we suppose to be the Bragg scatterer (see Figure 7). In this situation the bound wave doing the

scattering is more accurately described as a harmonic of the dominant wave and cannot be considered to exist on the leeward face of the dominant wave or to have a mean tilt angle. We will discuss in more detail below how we treat this situation, but, for now, we note that it is encountered for our geometry and scattering conditions primarily at friction velocities below about 0.2 m/s.

Composite-surface theory states that

$$\sigma_o = 16\pi k_o^4 \int |g_p'(\theta', s_c)|^2 \times \psi(2k_o \sin\theta', 0) P(s_u, s_c) ds_u ds_c \quad (12)$$

where ψ is the short wave spectral density; $k_o = 2\pi/\lambda$ is the microwave number; $\theta' = \theta + s_u$ is the local incidence angle; s_u and s_c are long wave tilt angles in and out of the plane of incidence, respectively (in our case, up and cross tank); P is the probability distribution of these angles; and g_p' is a polarization dependent geometric factor:

$$g_v'(\theta') = g_v(\theta') \quad (13)$$

$$g_h'(\theta', \alpha) = g_h(\theta) + (s_c/\sin\theta')^2 g_v(\theta') \quad (14)$$

where

$$g_v = \frac{(\epsilon - 1)[\epsilon(1 + \sin^2\theta') - \sin^2\theta'] \cos^2\theta'}{\left(\epsilon\cos\theta' + \sqrt{\epsilon - \sin^2\theta'}\right)^2} \quad (15)$$

for vertical polarization and

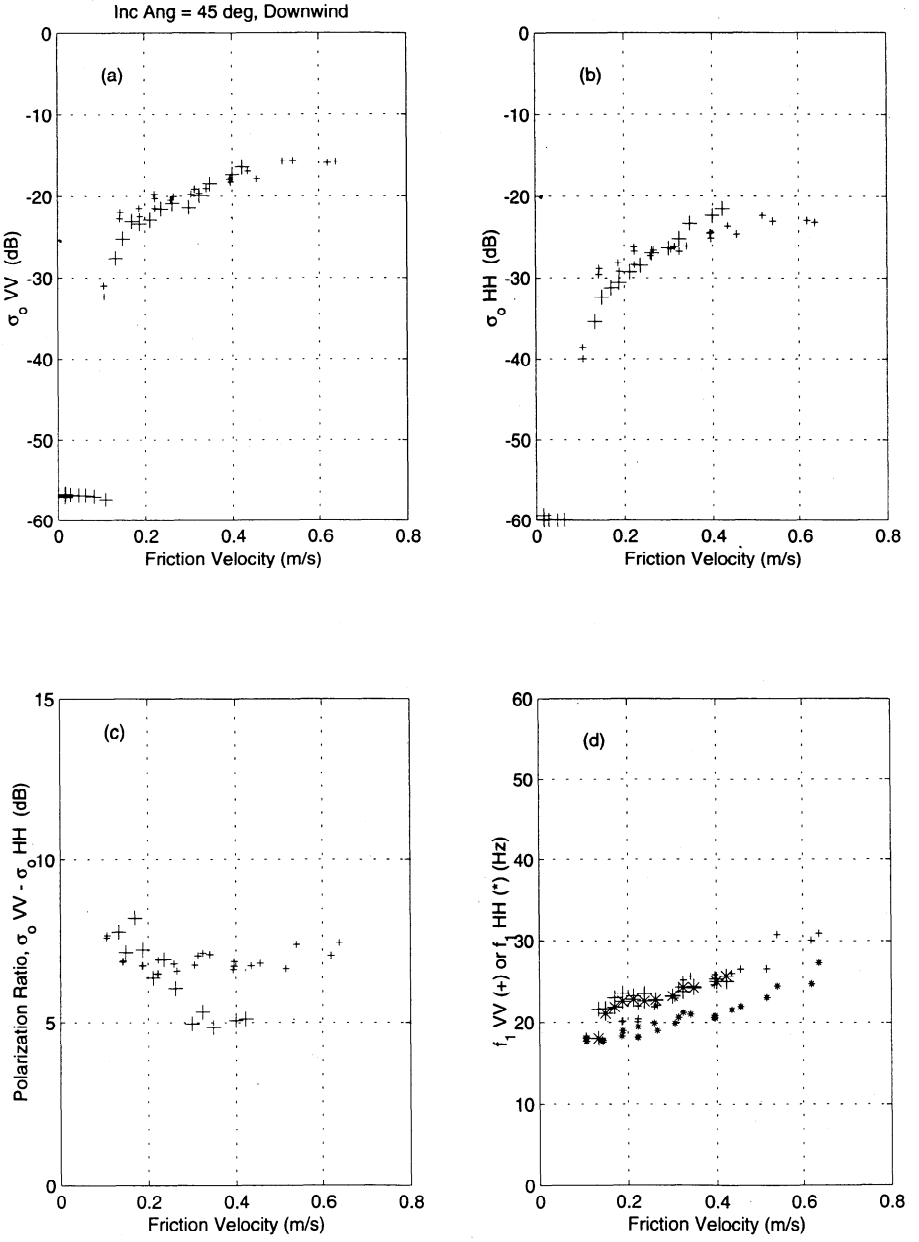

Figure 11. Same as Figure 10, except with antennas looking downwind.

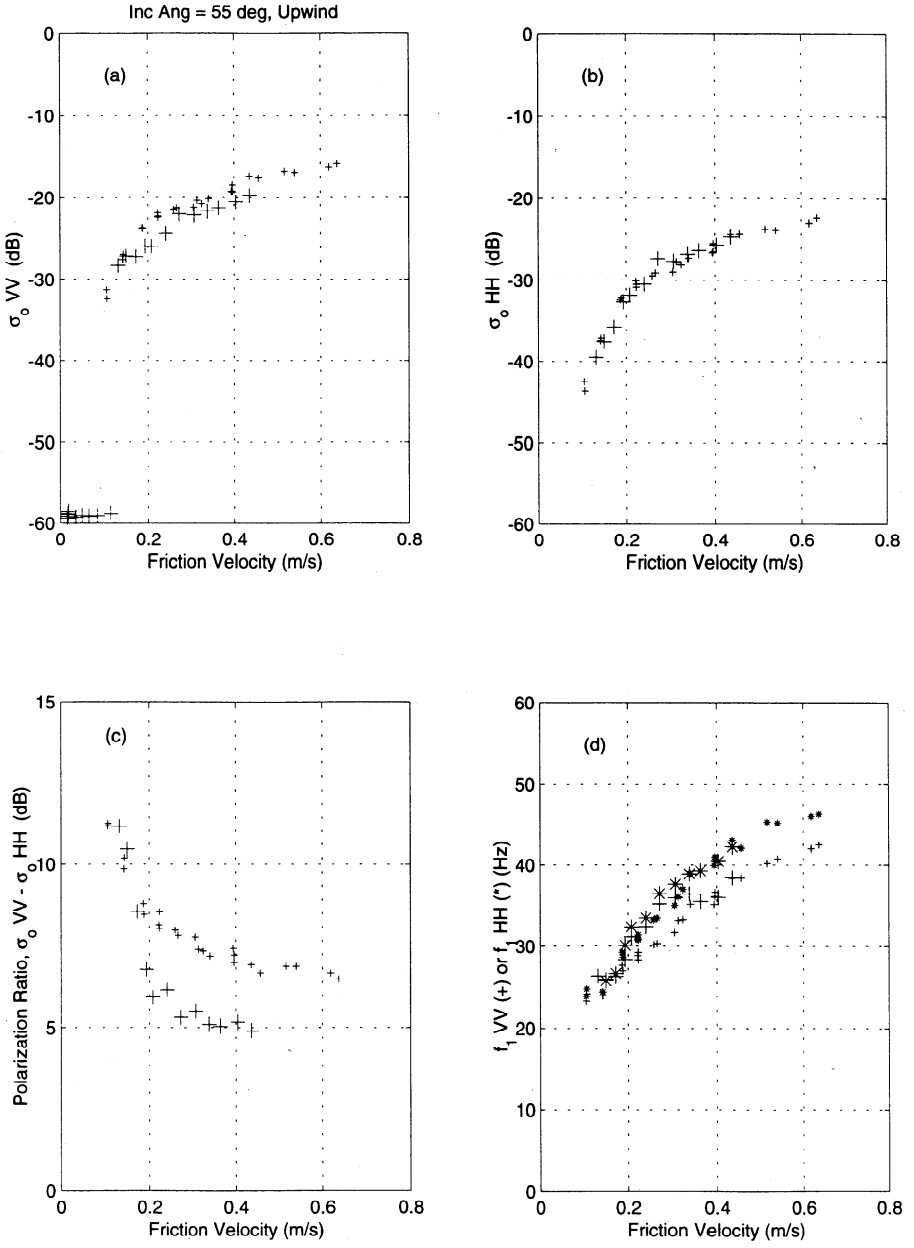

Figure 12. Same as Figure 10, except with a 55° incidence angle.

$$g_h = \frac{(\epsilon - 1)\cos^2\theta'}{\left(\cos\theta' + \sqrt{\epsilon - \sin^2\theta'}\right)^2} \tag{16}$$

for horizontal polarization and ϵ is the relative dielectric constant of the water.

Since $P(s_u, s_c)$ is given by (4) and we consider all conditional distributions to be Gaussian, we have

$$\begin{aligned}\sigma_o &= 16\pi k_o^4 \int |g_p'(\theta', \mathrm{Var}(s_c)_f)|^2 \\ &\times P_f \psi_f(2k_o \sin\theta', 0) P(s_u|f) ds_u \\ &+ 16\pi k_o^4 \int |g_p'(\theta_b', \mathrm{Var}(s_c)_b)|^2 \\ &\times P_b \psi_b(2k_o \sin\theta', 0) P(s_u|b) ds_u \end{aligned} \tag{17}$$

where subscripts f and b indicate either free or bound waves, and

$$\begin{aligned} P(s_u|x) &= [2\pi \mathrm{Var}(s_u)_x]^{-1/2} \\ &\times e^{-(s_u - < s_u >_x)^2/[2\mathrm{Var}(s_u)_x]} \end{aligned} \tag{18}$$

where x may be f or b. Note that the Bragg resonance condition at the peak of the probability distribution is slightly different from the normal condition due to the mean tilt, $< s_u >_x$:

$$k_B = 2k_o \sin(\theta + < s_u >_x). \tag{19}$$

While this is very close to the normal condition for the free waves, for the bound waves it is quite different

owing to their large mean slope. Thus a microwave Doppler spectrum should not be expected to resemble a cut through the spectrum shown in Figure 3 at the free Bragg wavenumber. Furthermore, the standard relationship between the Doppler shift produced by the Bragg wave and its frequency is different for a bound, tilted wave because the velocity of this wave is not parallel to its wavenumber. Thus the equation for the Doppler shift (9) for the bound, tilted wave becomes

$$f_d = f_b \left[\frac{\sin\theta'}{\sin(\theta + < s_u >_b)} \right]. \tag{20}$$

where f_b is the frequency of the bound, tilted wave. For $< s_u >_b = 0$ this reduces to the standard Bragg scattering relationship that the Doppler shift is the frequency of the Bragg wave.

In terms of the $B(k,0)$ values obtained from wave slope variance spectra from the scanning laser slope gauge,

$$P_f \psi_f(2k_o \sin\theta', 0) = B_f(2k_o \sin\theta', 0) \times (2k_o \sin\theta')^{-4} \tag{21}$$

$$P_b \psi_b(2k_o \sin\theta', 0) = B_b(2k_o \sin\theta', 0) \times (2k_o \sin\theta')^{-4}. \tag{22}$$

which may be used in (17) to evaluate σ_o. We have determined the means and variances of slopes for all probability distributions, except we have not been able to separate the total cross-tank slope into bound and free parts. Since the mean of the total cross-tank slope is nearly zero, we can assume that all cross-

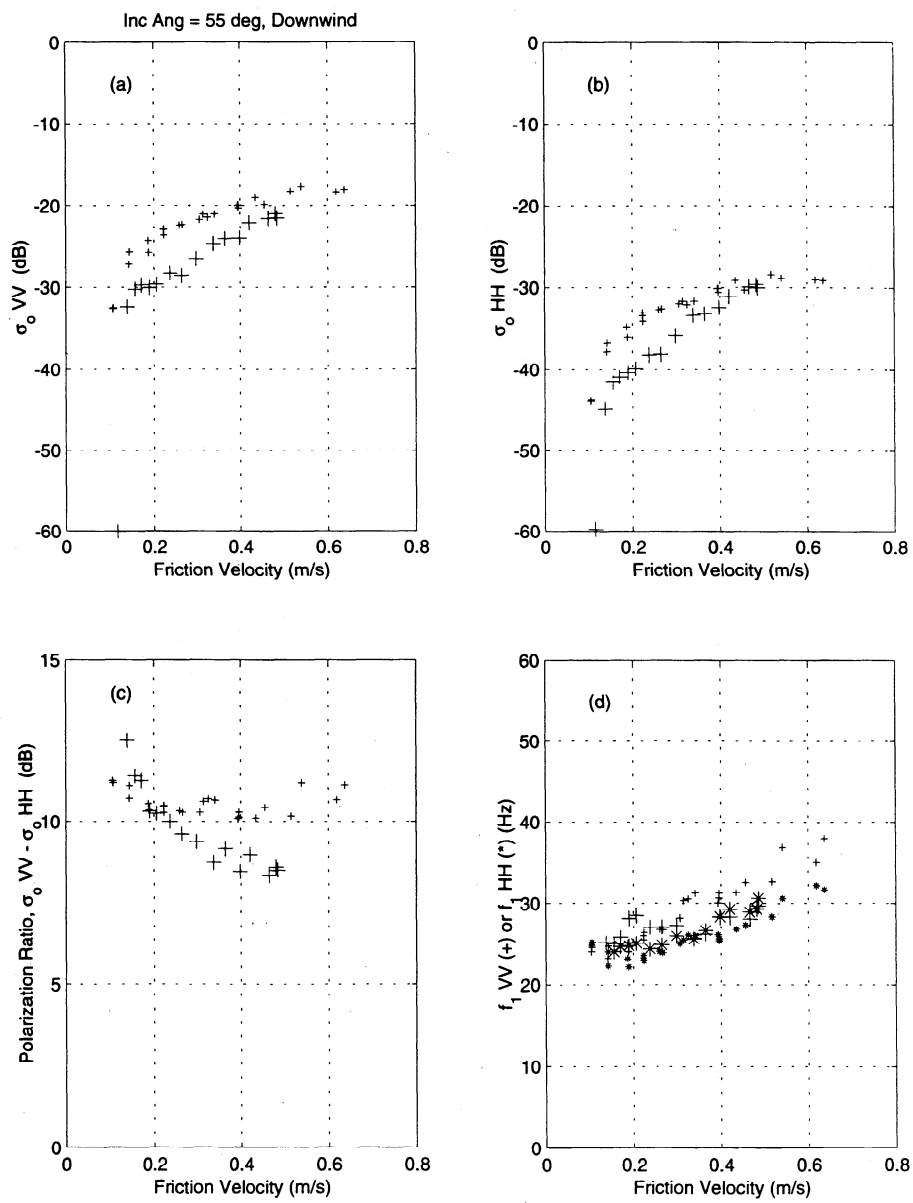

Figure 13. Same as Figure 10, except with a 55° incidence angle and antennas looking downwind.

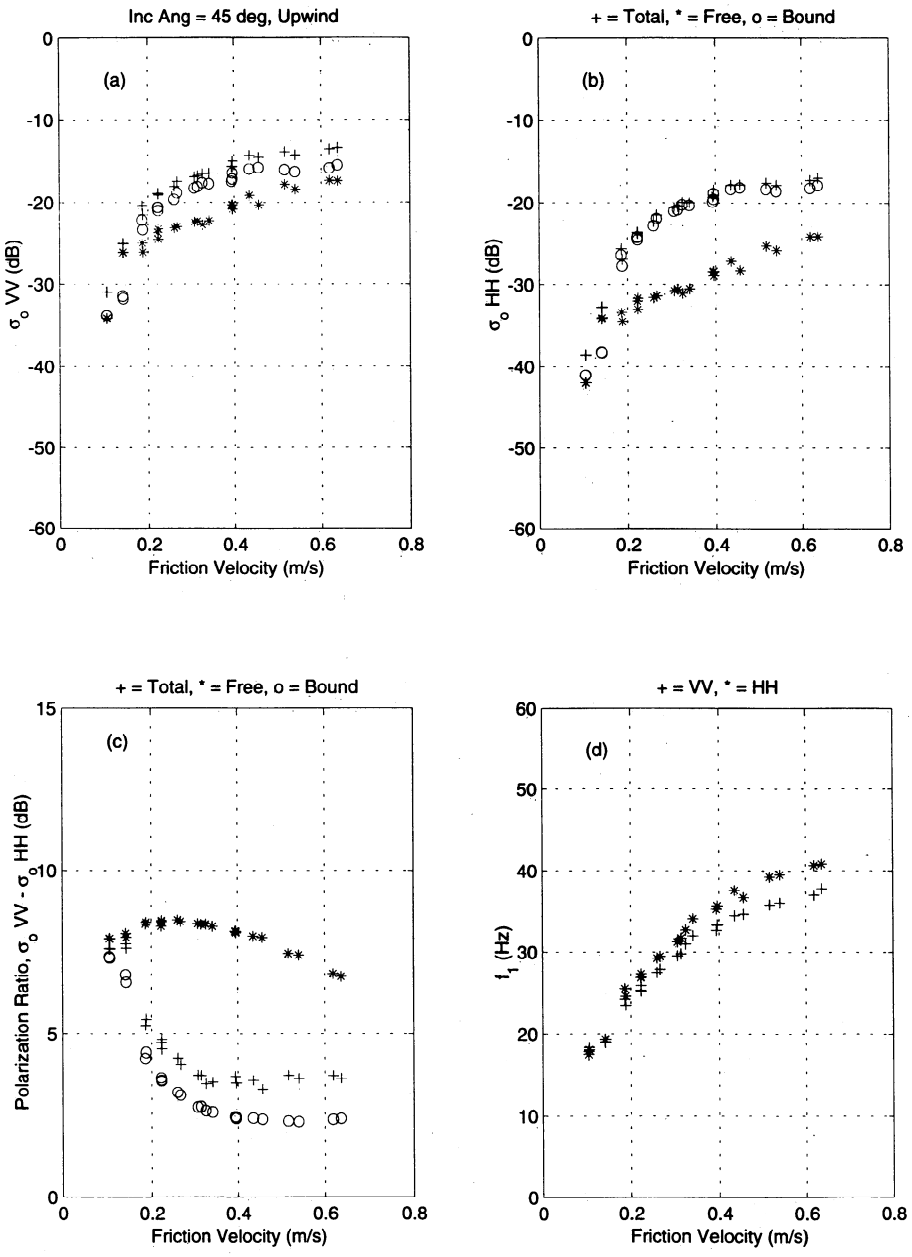

Figure 14. Microwave backscatter variables produced by the model based on a Bragg/composite-surface scattering theory including free or bound waves or both. (a) σ(VV), (b) σ(HH), (c) σ(VV)/σ(HH), and (d) f_1. In Figures 14a–14c, asterisks denote only free waves; circles, only bound waves; and pluses, both free and bound waves. In Figure 14d, asterisks are HH and pluses are VV. The incidence angle is 45°, and the antennas looked upwind. The format is the same as Figures 10 through 13, where the predictions of total scatter are reproduced as small symbols.

tank mean slopes are zero to a good approximation, so that the only quantities still needed to evaluate (17) are $\mathrm{Var}(s_c)_f$ and $\mathrm{Var}(s_c)_b$. We may use (8) to obtain a relationship between these variances. In order to close the equations, we will assume that the ratio $\mathrm{Var}(s_c)_f/\mathrm{Var}(s_c)_b = \mathrm{Var}(s_u)_f/\mathrm{Var}(s_u)_b$. Calling this ratio α, (6) yields

$$\mathrm{Var}(s_c)_b = \frac{\mathrm{Var}(s_c)}{\alpha P_f + P_b} \tag{23}$$

$$\mathrm{Var}(s_c)_f = \alpha\ \mathrm{Var}(s_c)_b. \tag{24}$$

We have now determined all parameters necessary to compute σ_o using (17). The lines in Figures 4 and 6 show the fits to the data that we have used to evaluate these parameters and the results of calculating σ_o are shown in Figures 14a–14c through 17a–17c. In Figures 14d, 15d, 16d, and 17d, we show the first moments of the Doppler spectra. These were computed by assuming that the bound and free wave parts of the Doppler spectra were symmetric about the frequencies given by (9) and (10) with the Bragg and dominant wave phase speeds, c_B and c_D, respectively, substituted for V. Thus

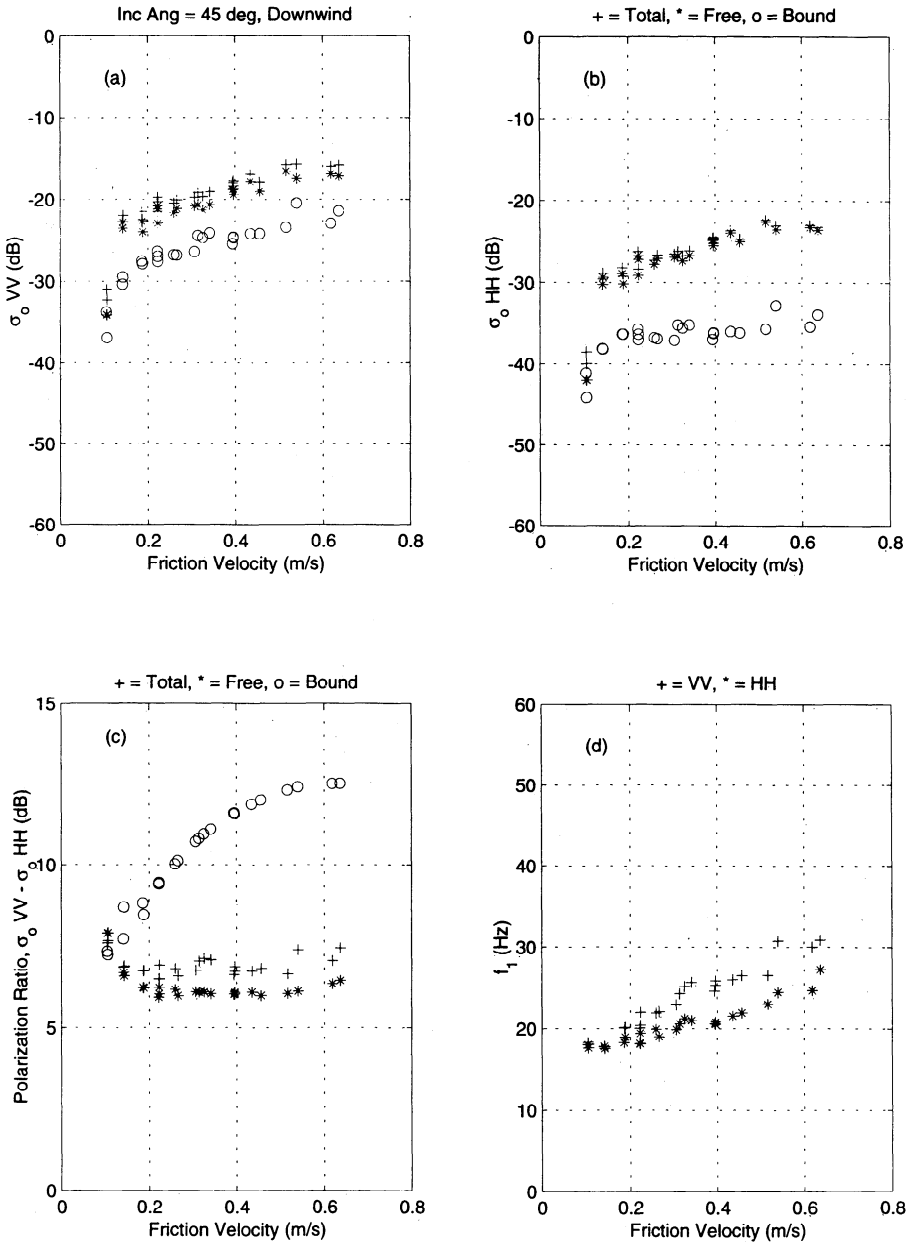

Figure 15. Same as Figure 14, except with antennas looking downwind.

$$f_1 = 2(\sigma_{of} c_B + \sigma_{ob} c_D) \sin\theta/(\lambda\sigma_o) \quad (25)$$

where σ_{of} is given by the first term in (17) and σ_{ob} is the second. This formulation assumes that there is no bias in the average speed of the free waves due to their absence in front of steep dominant wave crests or their possible modulation by longer waves. We expect changes in the mean speed of the free waves due to these effects to be small, however, and this seems to be supported by comparison of Figures 14d, 15d, 16d, and 17d with Figures 10d, 11d, 12d, and 13d.

A few further notes concerning the calculation of σ_o are in order. First, as mentioned above, at low wind speeds the dominant wavelength is not sufficiently long for the model to be valid for the longer bound waves. In these situations we have let $B(k,0)$ increase linearly from zero to the line shown in Figure 4 over the wavenumber range from 3 to 5 times the dominant wavenumber. As indicated above, this changed the calculations significantly only at friction velocities below 0.2 m/s and only for the upwind looks. The arrows in Figure 4 show the point at which $B(k,0)$ used in the calculations is within 3 dB of the curve in the figure, while the solid horizontal line shows the region from which 90% of the bound wave scattering comes for a 45° incidence angle upwind look. Second, we have used the full variances measured by the slope gauge in these calculations, even though these should include effects of waves too short to be considered "long" waves. We have done this because the factor by which these

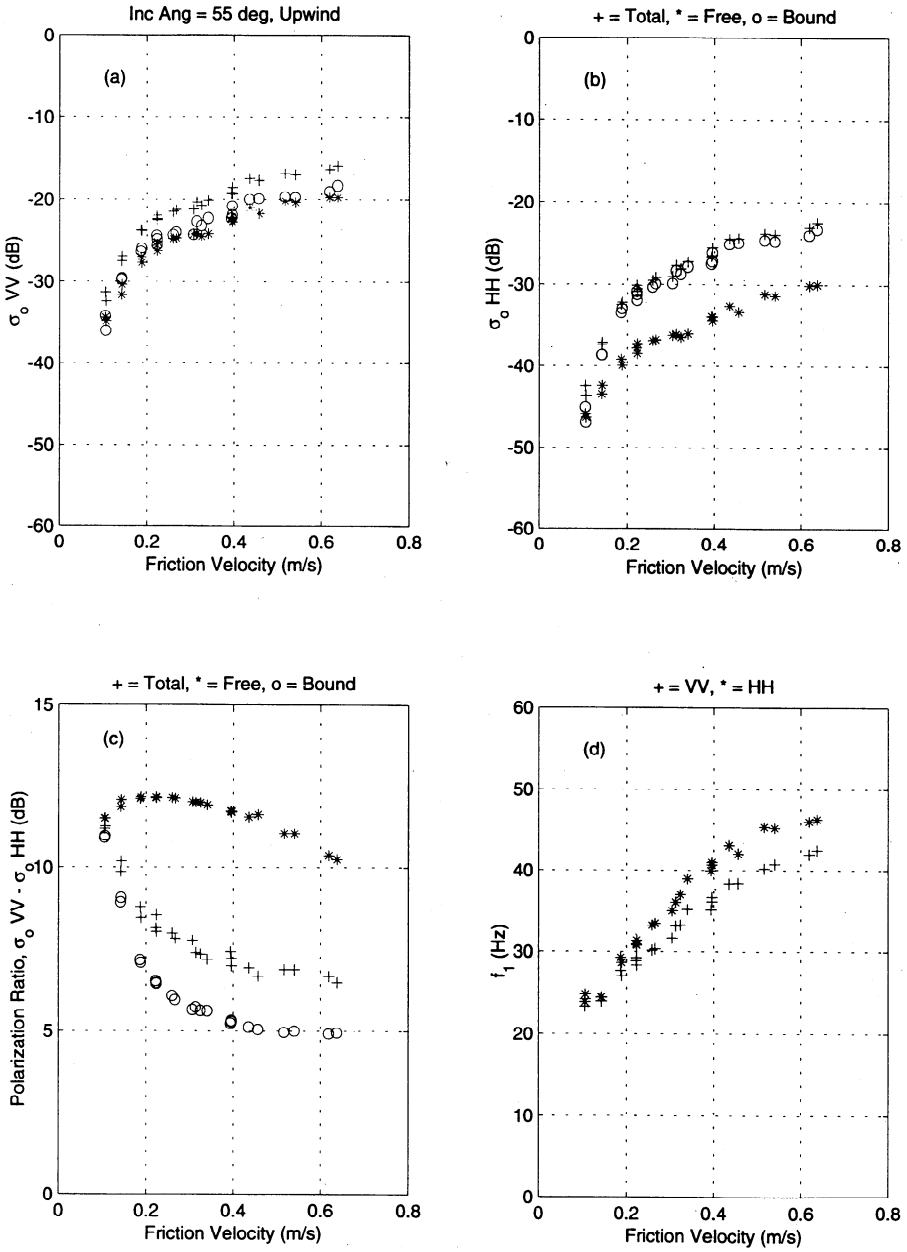

Figure 16. Same as Figure 14, except with a 55° incidence angle and the antennas looking upwind.

variances should be reduced is somewhat uncertain in a wave tank and because reductions to as little as 70% of the measured values had little effect on the calculations. Finally, we used different mean slopes for the bound waves when looking upwind than when looking downwind. The solid line in Figure 6e shows the values used when looking upwind, while the dashed line was used when looking downwind. The fetches at the microwave footprints on the water were 10 m for upwind looks and 12.5 m for downwind looks, while the slope was measured at a fetch of 14.3 m (see Figure 1). If we assume that the bound wave mean slopes required in the scattering model are the correct slopes, then this result suggests that the tilt of the bound waves may increase (decrease in magnitude) with fetch.

Figures 14 through 17 show that the model predicts many of the features of the data rather accurately. In Figures 14a–14c through 17a–17c we show the scattering that would be expected from freely propagating Bragg waves alone as asterisks and that from bound Bragg scatterers alone as circles. The pluses indicate the total backscatter expected and are reproduced as the small pluses in Figures 10a–10c through 13a–13c. In Figures 14d–17d and 10d–13d, the pluses give the first moments of VV polarized Doppler spectra while the asterisks give those for HH polarization. Again, theoretical values are reproduced in Figures 9 through 13 as the smaller symbols. Except for the cases of 55° downwind and the 1993 data at very high friction velocities, the predicted levels of backscatter are within 1 to 2 dB of those

measured. Comparing measured and modeled polarization ratios, we can see that the behavior is generally consistent. The modeled upwind polarization ratios show the large decrease with increasing wind speed, while the downwind ones decrease less than the upwind ones. Generally, the decrease in the modeled downwind polarization ratios is somewhat less than that actually observed and it tends to increase again at wind speeds above those observed. First moments of the Doppler spectrum given by the model when the antenna looks upwind are in very good agreement with the data. Not only is the increase with wind speed very close to that observed, but also f_1 for VV polarization falls below that for HH polarization at high wind speeds as observed. Looking downwind, the general rate of increase of f_1 from the model is close to that observed and smaller than in the upwind case, but HH and VV polarizations yield somewhat different values in contrast to the data. Overall, considering that most of the microwave data were collected 3 years after the wave spectra were obtained and at different fetches than either these spectra or the slope data, we feel that the agreement between model and data is very encouraging.

7. Conclusions

We have made measurements of wave slope variance spectra of short waves in a wind-wave tank using a scan-

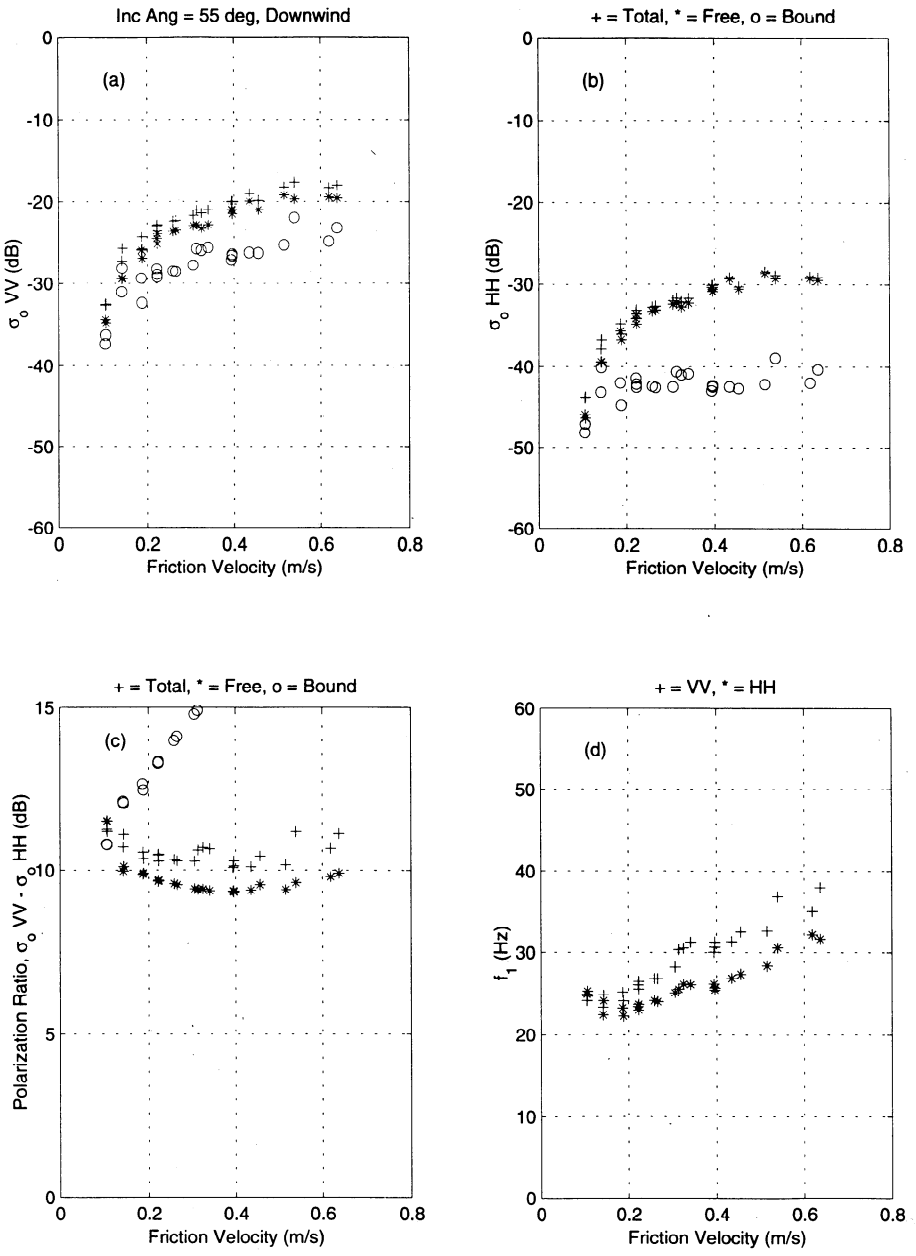

Figure 17. Same as Figure 14, except with a 55° incidence angle and the antennas looking downwind.

ning laser slope gauge, measured probability distributions of uptank and cross-tank surface slopes at a point, and obtained microwave Doppler information looking both upwind and downwind in the wave tank. All of these measurements contain evidence of the presence of waves that are bound to the dominant wave in the tank and propagate at its speed. We have shown that a consistent interpretation of these data is that both wind-generated waves and bound waves generated by the dominant waves are present in the tank. When the wavelength of the dominant wave is much longer than the bound waves, we have shown that our data can be explained by a model in which the turbulence associated with the bound waves suppresses wind-generated waves on the front, i.e., leeward, face of the dominant wave. We have shown that this interpretation can explain the probability of large, negative uptank slopes that we observed and can account, at least qualitatively, for the observed decrease in the probability of detecting bound waves at high wind speeds. Furthermore, by assuming that the bound waves backscattered incident microwaves according to Bragg/composite-surface scattering theory, we were able to account for many of the differences between the backscatter looking upwind and downwind. In particular, the model produced normalized cross sections very close to the measured values, showed the larger drop in the polarization ratio with increasing wind speed when looking upwind than when looking downwind, and yielded first moments of Doppler spectra that agreed well with the measurements, increasing more rapidly looking upwind than downwind.

In a separate work, *Plant* [1997] has shown that bound, tilted waves also appear to be present on the ocean but that their spectral densities are much smaller relative to the freely propagating, wind-generated waves in that case than they are in the wave tank. This is easily explained by the large slope of the dominant wave in the tank when compared to waves of similar lengths on the ocean [*Plant*, 1980]. This difference in spectral density means that bound, tilted waves play a much smaller role in microwave backscattering from the ocean than they do in wind-wave tanks. On the ocean their effects are observable primarily at large incidence angles where the backscatter from the free waves is small, especially at HH polarization. In a sense the microwave scattering community has been fortunate over the years to be able to explain so many features of backscatter from the ocean using a composite surface model based only on freely propagating waves. Had the bound waves been a bit larger, the scattering would have looked quite different.

Finally, we mention that we have not referred to the bound, tilted waves as parasitic waves because we do not believe that the connotation carried by this term necessarily applies to all the behavior we have observed. Parasitic waves as described by *Longuet-Higgins* [1963] and observed by *Perlin et al.* [1993] are generally thought to be capillary waves generated by longer waves through a resonance condition when the phase speeds of the two waves coincide. As *Longuet-Higgins* [1992] has commented, these waves appear to be distinct from the "crumpling" waves produced when short gravity waves break gently.

Acknowledgments. The authors would like to thank the staff of the National Water Research Institute, in particular, D.C. Beesley, who operated the wind-wave tank. The work was supported by NSF grant OCE 9402852AM01 and ONR grant N00014-93-1-0016.

References

Bock, E.J., and T. Hara, Optical measurements of capillary-gravity wave spectra using a scanning laser slope gauge, *J. Atmos. Oceanic Technol., 12*, 395–403, 1995.

Duncan, J.H., V. Philomin, M. Behres, and J. Kimmel, The formation of spilling breaking water waves, *Phys. Fluids, 6*, 2558–2560, 1994a.

Duncan, J.H., V. Philomin, H. Qiao, and J. Kimmel, The formation of a spilling breaker, *Phys. Fluids, 6*, S2, 1994b.

Duncan, J.R., W.C. Keller, and J.W. Wright, Fetch and wind speed dependence of Doppler spectra, *Radio Sci., 9*, 809–819, 1974.

Ebuchi, N., H. Kawamura, and Y. Toba, Fine structure of laboratory wind-wave surfaces studied using an optical method, *Boundary Layer Meterol., 39*, 133–151, 1987.

Ebuchi, N., H. Kawamura, and Y. Toba, Physical processes of microwave backscattering from laboratory wind wave surfaces, *J. Geophys. Res., 98*, 14,669–14,681, 1993.

Hara, T., E.J. Bock, and M. Donelan, Frequency-wavenumber spectrum of wind-generated gravity-capillary waves, *J. Geophys. Res., 102*, 1061–1072, 1997.

Jähne, B.K., and K.S. Riemer, Two-dimensional wave number spectra of small-scale water surface waves, *J. Geophys. Res., 95*, 11,531–11,546, 1990.

Keller, M.R., B.L. Gotwols, W.J. Plant, and W.C. Keller, Comparisons of optically-derived spectral densities and microwave cross sections in a wind-wave tank, *J. Geophys. Res., 100*, 16,163–16,178, 1995.

Kwoh, D.S., and B.M. Lake, The nature of microwave backscattering from water waves, in *The Ocean Surface*, edited by Y. Toba and H. Mitsuyasu, pp. 249–256, D. Reidel, Norwell, Mass., 1985.

Longuet-Higgins, M.S., The generation of capillary waves by steep gravity waves, *J. Fluid Mech., 16*, 138–159, 1963.

Longuet-Higgins, M.S., Capillary rollers and bores, *J. Fluid Mech., 240*, 659–679, 1992.

Longuet-Higgins, M.S., New insights into breaking waves and bubble entrainment, in *Sea Surface Sound '94*, edited by M.J. Bickingham and J.R. Potter, pp. 159–173, World Sci., River Edge, N.J., 1994.

Longuet-Higgins, M.S., and R.P. Cleaver, Crest instabilities of gravity waves, 1, The almost highest wave, *J. Fluid Mech., 258*, 115–129, 1994.

Okuda, K., S. Kawai, M. Tokuda, and Y. Toba, Detailed observation of the wind-exerted surface flow by use of flow visualization methods, *J. Oceanogr. Soc. Jpn, 32*, 53–64, 1976.

Perlin, M., H. Lin, and C.L. Ting, On parasitic capillary waves generated by steep gravity waves: An experimental investigation with spatial and temporal measurements, *J. Fluid Mech., 255*, 597–620, 1993.

Plant, W.J., On the steady-state energy balance of short gravity wave systems, *J. Phys. Oceanogr., 10*, 1340–1352, 1980.

Plant, W.J., A model for microwave Doppler sea return at high incidence angles: Bragg scattering from bound, tilted waves, *J. Geophys. Res., 102*, 21,131–21,146, 1997.

Plant, W.J., and J.W. Wright, Phase speeds of upwind and downwind traveling short gravity waves, *J. Geophys. Res., 85*, 3304–3310, 1980.

Plant, W.J., W.C. Keller, R.A. Petitt Jr., and E.A. Terray, The dependence of microwave backscatter from the sea on illuminated area: Correlation times and lengths, *J. Geophys. Res., 99*, 9705–9723, 1994.

Rozenberg, A.D., D.C. Quigley, and W.K. Melville, Laboratory study of polarized scattering by surface waves at grazing incidence, I, Wind waves, *IEEE Trans. Geosci. Remote Sens., 33*, 1037–1046, 1995.

Wright, J.W., and W.C. Keller, Doppler spectra in microwave scattering from wind waves, *Phys. Fluids, 14*, 466–474, 1971.

E. Bock, Woods Hole Oceanographic Institution, Woods Hole, MA 02543.

M. A. Donelan, Rosenstiel School of Marine and Atmospheric Science, University of Miami, Miami, FL 33149.

T. Hara, Graduate School of Oceanography, University of Rhode Island, Narragansett, RI 02882.

V. Hesany, W. C. Keller, and W. J. Plant, Applied Physics Laboratory, University of Washington, 1013 N.E. 40th Street, Seattle, WA 98105. (plant@crosby.apl.washington.edu)

(Received March 30, 1998; revised September 28, 1998; accepted October 23, 1998.)